Acta Oceanol. Sin., 2024, Vol. 43, No. 5, P. 16–29
https://doi.org/10.1007/s13131-023-2295-x
http://www.aosocean.com
E-mail: ocean2@hyxb.org.cn

On the longitudinal shifts of the Agulhas retroflection point

Weiwei Zhang[1], Xiaoyi Yang[1, 2*], Wei Zhuang[1, 2], Xiaohai Yan[3, 4]

[1] State Key Laboratory of Marine Environmental Science, College of Ocean and Earth Sciences, Xiamen University, Xiamen 361002, China

[2] Southern Marine Science and Engineering Guangdong Laboratory (Zhuhai), Zhuhai 519082, China

[3] Center for Remote Sensing, College of Earth, Ocean and Environment, University of Delaware, Newark, DE 19716, USA

[4] Joint Center for Remote Sensing, University of Delaware-Xiamen University, Newark, DE 19716, USA and Xiamen 361002, China

Received 20 November 2023; accepted 24 January 2024

© Chinese Society for Oceanography and Springer-Verlag GmbH Germany, part of Springer Nature 2024

Abstract

The Agulhas system is the strongest western boundary current system in the Southern Hemisphere and plays an important role in modulating the Indian-to-Atlantic Ocean water exchange by the Agulhas leakage. It is difficult to measure *in situ* transport of the Agulhas leakage as well as the Agulhas retroflection position due to their intermittent nature. In this study, an innovative kinematic algorithm was designed and applied to the gridded altimeter observational data, to ascertain the longitudinal position of Agulhas retroflection, the stability of Agulhas jet stream, as well as its strength. The results show that the east-west shift of retroflection is related neither to the strength of Agulhas current nor to its stability. Further analysis uncovers the connection between the westward extension of Agulhas jet stream and an anomalous cyclonic circulation at its northern side, which is likely attributed to the local wind stress curl anomaly. To confirm the effect of local wind forcing on the east-west shift of retroflection, numerical sensitivity experiments were conducted. The results show that the local wind stress can induce a similar longitudinal shift of the retroflection as altimetry observations. Further statistical and case study indicates that whether an Agulhas ring can continuously migrate westward to the Atlantic Ocean or re-merge into the main flow depends on the retroflection position. Therefore, the westward retroflection may contribute to a stronger Agulhas leakage than the eastward retroflection.

Key words: Agulhas system, Agulhas leakage, retroflection position, local wind stress curl

Citation: Zhang Weiwei, Yang Xiaoyi, Zhuang Wei, Yan Xiaohai. 2024. On the longitudinal shifts of the Agulhas retroflection point. Acta Oceanologica Sinica, 43(5): 16–29, doi: 10.1007/s13131-023-2295-x

1 Introduction

The Agulhas system is the boundary current system of the South Indian Ocean Subtropical Gyre. As the Agulhas Current (AC) flows southwestward to the south tip of Africa, it separates from the Agulhas Bank and becomes a free jet until reaching a turning point termed Agulhas retroflection (AR). Here, roughly 75% of AC (van Sebille et al., 2009a) returns to the Indian Ocean as the Agulhas Return Current (ARC), while the rest may enter the Atlantic as Agulhas leakage (AL). Recent study based on floats data shows that 27.8% of the AC water leaks into the Atlantic (Daher et al., 2020).

The AL is considered a crucial component of the Atlantic Meridional Overturning Circulation (AMOC) upper limb, and can affect the strength and stability of AMOC (Gordon, 1986; Biastoch et al., 2008, 2009; Gunn et al., 2020). The AL consists of Agulhas rings with diameters ranging from 150 km up to more than 300 km (de Ruijter et al., 1999; van Aken et al., 2003), smaller eddies (Wei and Wang, 2023), as well as submesoscale features (Loveday et al., 2015; Cheng et al., 2016). The Agulhas rings can be observed and tracked using altimetry data, and their sizes and translation speed can be inferred as well (Byrne et al., 1995; Schouten et al., 2000; Dencausse et al., 2010b; Backeberg et al., 2012), but its exact mass, heat, and salt transports are difficult to estimate (de Ruijter et al., 1999; van Aken et al., 2003). The mass and buoyancy transport of the total leakage is even harder to derive with *in situ* or altimeter observations. Therefore, the volume or heat transport associated with AL is often indirectly estimated based on the proportion of AC water entering the South Atlantic (Bryden et al., 2005). It should be noted that the large salinity variability of AC also makes it harder to quantify the AL salt transport (McMonigal et al., 2020).

The relationship between AL, AC, and the AR position remains unclear. On one hand, Rouault et al. (2009) and van Sebille et al. (2009a) have attempted to establish a statistical relationship between AC and AL, but their conclusions contradicted each other. Using a temperature and salinity criteria to determine AL water mass in numerical model, Rouault et al. (2009) found a positive correlation between AC and AL. Although the negative correlation between AC transport and AL (van Sebille et al., 2009a) agrees with most of previous understanding of the retroflection dynamics (Ou and de Ruijter, 1986; Dijkstra and de Ruijter, 2001; Le Bars et al., 2012), other studies using a hierarchy

Foundation item: The National Key R&D Program of China under contract No. 2019YFA0606702; the National Natural Science Foundation of China under contract Nos 42176222, 91858202, 41630963, and 41776003; the National Science Foundation under contract No. NSF-IIS-2123264; the fund suported by the National Aeronautics and Space Administration under contract No. NASA-80NSSC20M0220.

*Corresponding author, E-mail: xyyang@xmu.edu.cn

of numerical models have shown that the AL may be decoupled from the AC (Loveday et al., 2014), but responds strongly to the changes in wind stress curl of the westerlies (Durgadoo et al., 2013). On the other hand, the relationship between ring shedding, the AL strength, and the AR longitudinal position has been established (Ou and de Ruijter, 1986; van Sebille et al., 2009b), and the AR position was even used as proxy of the ring shedding events or the AL (Lutjeharms and Van Ballegooyen, 1988; Feron et al., 1992).

Earlier algorithms used to identify the AR position as well as the related ring-shedding processes are mostly based on the specific sea surface height (SSH) or absolute dynamic topography (ADT) contours. For instance, Dencausse et al. (2010a) used the westernmost point from one of the two SSH isolines, depending on the distance between the westernmost points of the two isolines. Usually, the 1.7 m isoline is used to determine retroflection position. At the moment of ring shedding, however, the distance between 1.7 m and 1.9 m SSH contours may be more than 150 km. Then a higher critical value of 1.9 m is applied to avoid ambiguity in definition. Van Sebille et al. (2009b) used the SSH isoline on which the maximum AC velocity was found, and took its westernmost point as the retroflection. Loveday et al. (2014) set a threshold of the mean SSH within the upstream AC area where it is less turbulent, thus obtained an isoline whose westernmost point is considered the retroflection. Based on satellite altimetry data, Zhu et al. (2021) used 0.7 m ADT isoline to detecting the Agulhas retroflection. In addition to the various isoline-related morphological criteria, Russo et al. (2021) further proposed an improved method to ascertain the retroflection, by combining the kinematical feature, i.e., the maximum speed of the current with its associated ADT values. Once the retroflection is determined, its variability on multiple timescales can be analyzed. However, no long-term retroflection longitudinal changes were confirmed during the altimeter era, but seasonality has been noted and the seasonality phases have shown strong interannual variability (Dencausse et al., 2010a).

High eddy kinetic energy has been observed as well as simulated in the vicinity of the retroflection area (Loveday et al., 2014; Cheng et al., 2016), and both cyclonic and anticyclonic eddies can interact with the AR (Lutjeharms et al., 2003). Ring shedding events in infrared images tend to be accompanied by abrupt eastward jump of the retroflection point, usually following an accelerating westward penetration of AC jet (Lutjeharms and Van Ballegooyen, 1988). This phenomenon was also observed by Feron et al. (1992) and Dencausse et al. (2010a) from sea surface ADT, and was subsequently termed as “pulse-like” behavior of the retroflection. Dencausse et al. (2010a) also noted abrupt westward jump of the retroflection, due to re-absorption of a previously detached ring. Cyclonic lee eddies are present west of the Agulhas Bank, and may contribute to the westward elongation of the retroflection through advection (Dencausse et al., 2010a). Lutjeharms et al. (2003) observed a lee eddy splitting into two, and found it instrumental in pinching the Agulhas ring off the retroflection.

Given the wide divergence about the linkage of AL with AC and the complexity of retroflection dynamics, here we propose a new algorithm to detect the retroflection locations so as to reexamine the relationship between retroflection and upstream AC. The impact of the local wind forcing on the AR and the linkage of AR position with ring shedding processes and the AL are also involved. In Section2, the gridded altimeter data and a regional numerical model configurations are described, and the energetics of the Agulhas system is analyzed to identify the AC jet core and the retroflection. The relationship between the AC jet and the AR position is examined in Section 3. Section 4 shows the AR displacements in details, and local wind forcing anomaly associated with displacements is noted. Numerical experiments are designed to test the impact of the local wind anomaly on the AR in Section 5. The ring shedding, occlusion and migration processes are discussed for extreme eastward and westward retroflection events in Section 6. Finally, the results are summarized and discussed in Section 7.

2 Data and methods

2.1 *Data*

To examine the circulation characteristics around the retroflection point, the delayed-time daily L4 global ADT and sea level anomaly (SLA) data produced by Data Unification and Altimeter Combination System (DUACS) was used (Taburet et al., 2019). The dataset has a (1/4)° × (1/4)° resolution with time period ranging from January 1993 to December 2018. This dataset is generated under the framework of the Copernicus Climate Change service, using two altimeters for mesoscale signal retrieval. The reference missions are Ocean Topography Experiment (TOPEX)-Poseidon, Jason-1, Jason-2 and Jason-3. The ADT is derived from the SSH plus the CNES-CLS18 global mean dynamic topography, which is produced by combining the GOCO05S model (a satellite-only global gravity field model computed by the Gravity Observation Combination (GOCO) project) with *in situ* measurements, the Gravity Field and Steady-State Ocean Circulation Explorer (GOCE) mission data, and 10.7-year Gravity Recovery and Climate Experiment (GRACE) data (Rio and Santoleri, 2018; Mulet et al., 2021). The SLA is derived by removing the 1993–2012 mean sea surface from the sea surface height measured by the altimeter (Taburet et al., 2019).

The daily wind stress is computed from the 10-meter wind field of ERA5 (the fifth generation of European Centre for Medium-Range Weather Forecasts (ECMWF) atmospheric reanalysis of the global climate) dataset (Hersbach et al., 2020). The Integrated Forecasting System Cy41r2 was used to generate the ERA5 reanalysis data. The forecasting system includes atmosphere, land, ocean, and a hybrid incremental 4D-Var data assimilation component. The data covers the period from January 1979 to present, with a spatial resolution of (1/4)° × (1/4)°.

The monthly sea surface temperature (SST) of ERA5 dataset and the Optimum Interpolation SST (OISST) analysis product (Reynolds et al., 2007) were also used in this study.

2.2 *Numerical experiments*

A regional ocean model system (ROMS) of version 3.7 was used to test possible effects of local forcing on the AR longitudinal shifts. ROMS is a free-surface terrain-following hydrostatic model based on primitive equations (Haidvogel et al., 2000; Marchesiello et al., 2003), which are solved by split-explicit time-stepping (Shchepetkin and McWilliams, 2005). The model domain spans from 48°S to 8°S, and 20.2°W to 69.9°E, and it has 40 vertical levels. The horizontal grid size increases from 7.7 km at 48°S to 11.1 km at 8°S. Third order upstream bias scheme is used for horizontal advection, and fourth order centered scheme is used for vertical advection. The harmonic horizontal mixing scheme is used. The eddy viscosity and eddy diffusivity coefficients are scaled by grid area, and their maxima are 10 m^2/s and 2 m^2/s respectively. ROMS includes several vertical mixing schemes (Warner et al., 2005), and the Mellor-Yamada level 2.5 turbulent closure is used in this study. The ERA5 turbulent surface stress, surface net radiation flux, and the surface net heat flux data are mapped to the model grid and to force the numerical model (Hersbach et al., 2020). The data from an unperturbed

control member of the Ocean Reanalysis System 5 (ORAs5) is mapped onto the model grid to provide boundary and initial conditions for the numerical simulations.

2.3 *Identification of the AC jet path and retroflection point*

The monthly mean kinetic energy (MKE) and the eddy kinetic energy (EKE) were calculated based on daily geostrophic velocities derived from the satellite altimetry data and their anomalies. The formulas are shown as follows:

$$\mathrm{MKE} = 0.5 \times \left(\overline{u}^2 + \overline{v}^2\right), \tag{1}$$

$$\mathrm{EKE} = 0.5 \times \overline{\left(u'^2 + v'^2\right)}, \tag{2}$$

where the overbars denote the monthly time mean and the primes are the deviations from the monthly mean field.

The climatologies of MKE and EKE patterns are shown in Figs 1a and b, respectively. Unsurprisingly, the maximum MKE is along the AC and ARC cores, while the EKE is stronger in the retroflection area and the ARC meandering area. In light of their distinct kinematic features, the AC, ARC, and the AR can be easily distinguished by contrasting the difference between MKE and EKE (Fig. 1c). MKE is much larger than EKE along the AC path, while the difference becomes negative where AL originates at the retroflection point. Although both MKE and EKE are strong in the ARC meandering area, their difference is moderately high. In the Agulhas ring spawning area, the EKE is stronger than MKE during the entire study period, and the two are significantly correlated as well (Fig. 1d).

Since the AC manifests as a remarkably large difference between MKE and EKE (Fig. 1c), a dynamic algorithm was designed to identify the AC jet path. First, the monthly mean MKE and EKE were calculated from geostrophic currents within the latitudes of 25°S and 41°S. Then the maximum of difference (null if less than 0.1 m^2/s^2) between MKE and EKE was searched along each available meridian from 0°E to 45°E, and the location of the maximum was considered the AC jet path at the corresponding longitude. Each segment of the AC jet path should include at least 4 consecutive grid points in either meridional or zonal direction, to prevent mistaking mesoscale or smaller scale features as currents. Here the AC jet path represents where the strongest current is located, and it does not take the width of the AC into account, thus it is not to be confused with the AC transport integrated across a chosen section in a previous study by Beal and Elipot (2016).

3 Relationship between the AC strength, its stability, and the retroflection displacement

The resultant monthly AC jet axis is shown in Fig. 2. It is found to be more stable upstream (smaller variation) close to the continent and less stable downstream (larger variation) after separating from the southern tip of Africa, roughly divided at 26°E (dashed line in Fig. 2). The mean path orientation turns from southwestward east of 20°E to westward around 18°E, and tilts further northwestward around 16°E (thick black line in Fig. 2). It should be noted that the mean jet path is an average taken at each available longitude. The sample size for the mean latitude calculation decreases towards west, thus the northward slant of AC path west of 17°E may not be robust in statistics. Nonetheless, the mean AC path derived from the dynamical algorithm generally accords with the direction of ADT isolines and fits the route along the maximum ADT gradient, which fully demonstrates the rationality of this method.

The difference between MKE and EKE are integrated along the upstream and downstream sections of the AC jet path to represent the AC strength, and their normalized indices and 13-

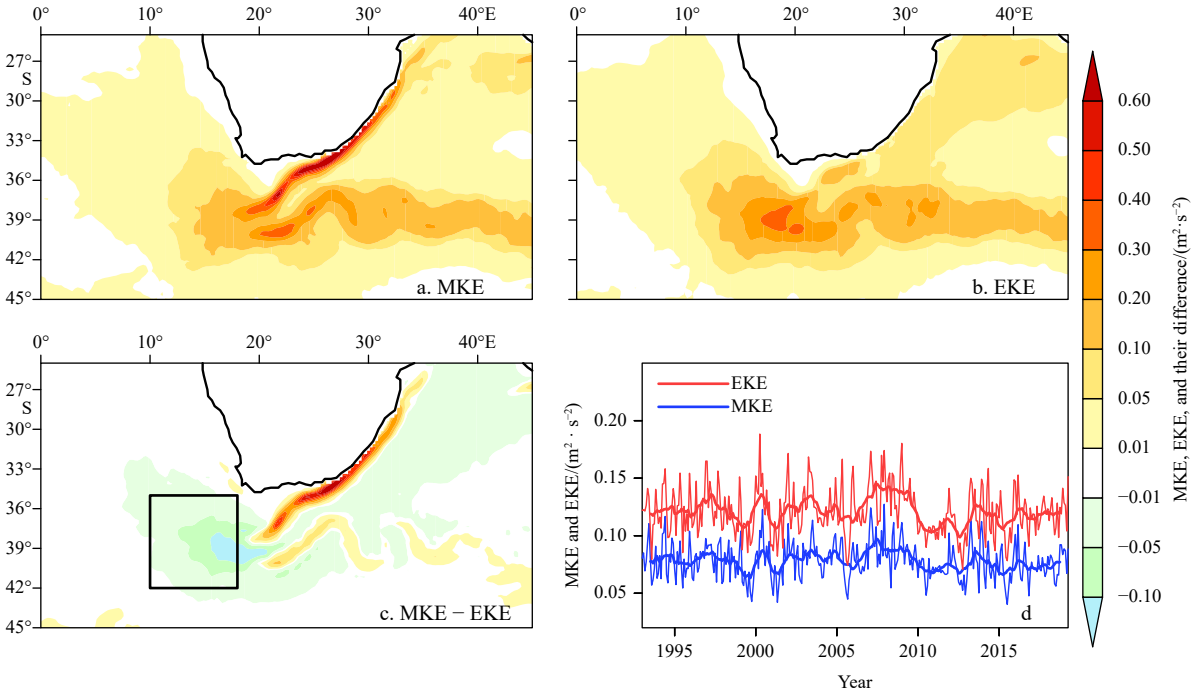

Fig. 1. The climatology of mean kinetic energy (MKE) (a) and eddy kinetic energy (EKE) (b) in the Agulhas system during 1993 to 2018, which is computed using the geostrophic velocity from the gridded L4 satellite altimetry product, the difference between MKE and EKE (c), and the time series of EKE and MKE in the black rectangular box (35°–42°S, 10°–18°E) in c, which denotes the region where MKE is much less than EKE and is roughly the origin of Agulhas leakage as well (d). The thick red and blue lines in d are the 13-month running mean of the MKE and EKE.

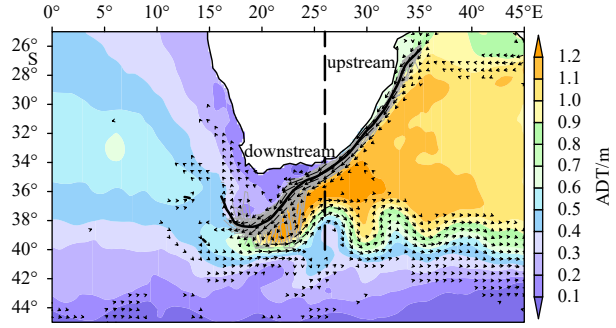

Fig. 2. The climatology of absolute dynamic topography (ADT) (colored shading), and the corresponding geostrophic velocity (black vectors) during the period of January 1993–December 2018. The thick black line is the mean location of the Agulhas Current jet path derived for each available longitudinal grid (with (1/4)° increment). The grey lines are all the identified Agulhas Current jet path. The dashed black line at 26°E approximately divides the Agulhas Current jet path into upstream and downstream sections. It is noted that the variation of the paths gets much higher downstream.

month running means are shown in Figs 3a and b. It should be noted that the along-path integration is different from that along a vertical section across the AC, which only reflects its strength at a certain point along its path. The correlation coefficients between upstream and downstream jet strength are 0.33, 0.49, and 0.58 (all significant at 95% level of t-test), respectively for monthly, 3-month running average, and the 13-month running average. This shows somewhat consistency between the upstream and downstream flow strengths.

In order to quantify the swing amplitude of the AC downstream path, the distance between each AC paths (the grey lines in Fig. 2) and the mean (the thick black line in Fig. 2) is measured by computing the spatial standard deviation (std) along the AC downstream. The formula is as follows:

$$\mathrm{std} = \sqrt{\frac{1}{n}\sum_{i=1}^{n}(x_i - \bar{x})^2}, \tag{3}$$

where x_i and $\bar{x}$ denote the latitude values at each longitude points for individual and time mean paths respectively, and n is the total downstream longitude number. The time series is presented in Fig. 3c. At downstream, the jet path alteration is highly correlated with its strength with the correlation coefficients of –0.58, –0.69, and –0.69 (all significant at 95% level of t-test), for monthly, 3-month, and 13-month running means. Therefore, on seasonal to interannual timescales, the stronger the downstream AC jet, the more stable (i.e., the less variable) it is.

A few studies have looked into the relationship between the AC transports and the longitudinal position of retroflection point. On one hand, Ou and de Ruijter (1986) found that a stronger AC has greater inertia, thus it can detach from the continental slope more easily, indicating the eastward shift of retroflection point. Based on (1/10)° numerical simulations, van Sebille et al. (2009a, b) also found that weaker AC corresponds to further westward retroflection displacements. On the other hand, using a series of sensitivity numerical experiments, Loveday et al. (2014) showed that the AL did not respond to increasing AC strength driven by increasing trade wind stress curl, and consequently concluded that AL was decoupled from the AC. They also noted that

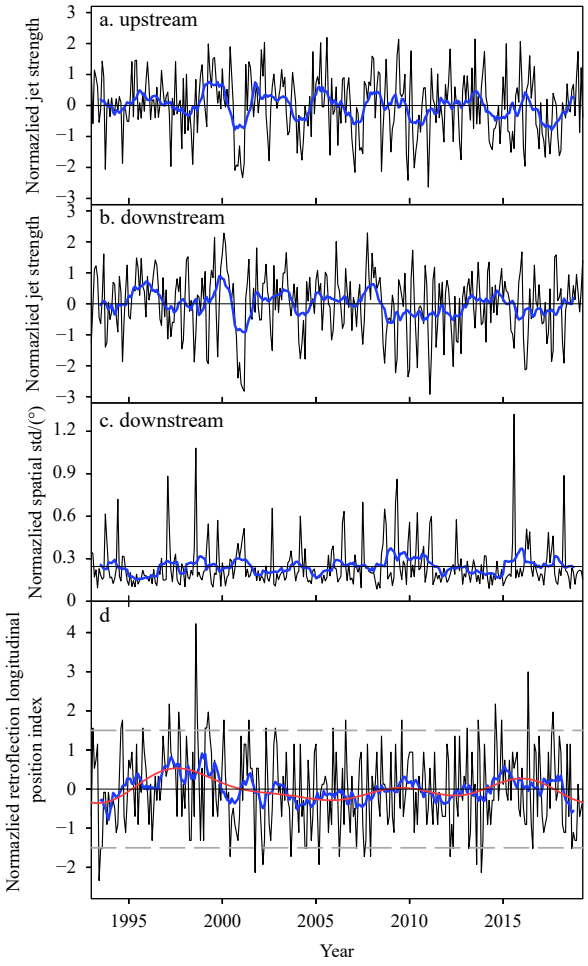

Fig. 3. Normazlied monthly time series for various physical factors. a. AC strength integrated along the upstream AC jet path (black line) and its 13-month moving average (blue line). b. Same as a, but integrated along the downstream AC jet path. c. Spatial standard deviation (std) along the downstream jet path, the black and the blue lines represent monthly and 13-month running mean, respectively. d. Normalized longitudinal displacement of the retroflection point, which is defined as the westernmost longitude of the AC jet path. The black , blue, and red lines denote the monthly, the 13-month running mean, and the 5-year low-pass filtered displacements, respectively. The grey dashed lines indicate ±1.5 standard deviations from the mean displacements, which is the thresholds for composite analyses. The normalization of the time series is achieved following the formula as $i = \frac{x-\mu}{\sigma}$, where μ is the climatological mean and σ is the standard deviation of x.

stronger inertial AC overshoot did not result in more eastward retroflection. In our study, the retroflection point is recognized as the westernmost end-point of the AC jet stream. The normalized retroflection longitudinal position index (Fig. 3d) is compared with the upstream and downstream AC jet strength and its stability. The retroflection longitude is not significantly correlated with the integrated AC jet strength upstream or downstream, and it is not significantly correlated with the downstream jet stability either. Therefore, our results do not support the linear correlation between the AC and the AR position, which is in line with Loveday et al. (2014).

4 Extreme retroflection events

Given decoupling of the retroflection position from the AC strength, composite analysis based on the ±1.5 standard deviation of normalized retroflection position index shown in Fig. 3d is applied to ascertain factors that account for the east-west shift of retroflection. Extreme eastward retroflection displacements (otherwise known as early retroflections), i.e., more than 1.5 standard deviation east of the mean longitude, are found to occur in 24 months out of the total 312 months considered in this study. Similarly, the extreme westward displacements (otherwise known as late retroflections) are found to occur in 21 months. The jet paths for the 21 most westward months and 24 most eastward months are displayed in Figs 4a and b, respectively. In the case of the extreme westward displacements, the jet paths are elongated westward until about 16°E and occasionally tilt northward. For the extreme eastward displacements, the jet paths shoot southward at about 21°E.

The composites of the ADT and geostrophic flow for the extreme eastward and westward retroflections differ from each other (Fig. 5). A weak anticyclonic feature is located to the west of the extreme eastward retroflection point (Fig. 5a), alluding to the ring shedding process associated with the eastward shift of AC. As for the extreme westward cases, it is noteworthy that a remarkable cyclonic feature with low ADT values appears to the north of the elongated AC jet paths (Fig. 5b). Unlike other types of cyclonic eddies, such as those induced by Natal Pulses or shear edge eddies on the east side of the Agulhas Bank (Lutjeharms et al., 2003), this cyclonic feature occurs locally on the west side of the Agulhas Bank and coincides with the elongated AC, and is larger in size than the shear edge eddies.

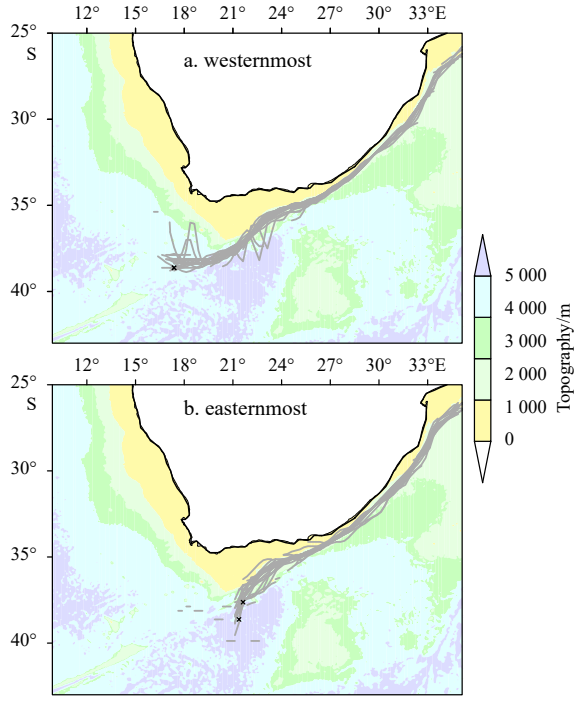

Fig. 4. The ETOPO1 bottom topography in colored shadings overlapped with the 21 westernmost AC jet paths (a) and the 24 easternmost AC jet paths (b), with ±1.5 standard deviation of the retroflection longitudes as selecting criteria, respectively. The black crosses denote the final retroflection points for each path according to our algorithm. ETOPO1 is a 1 arc-minute global relief model of Earth's surface that integrates land topography and ocean bathymetry.

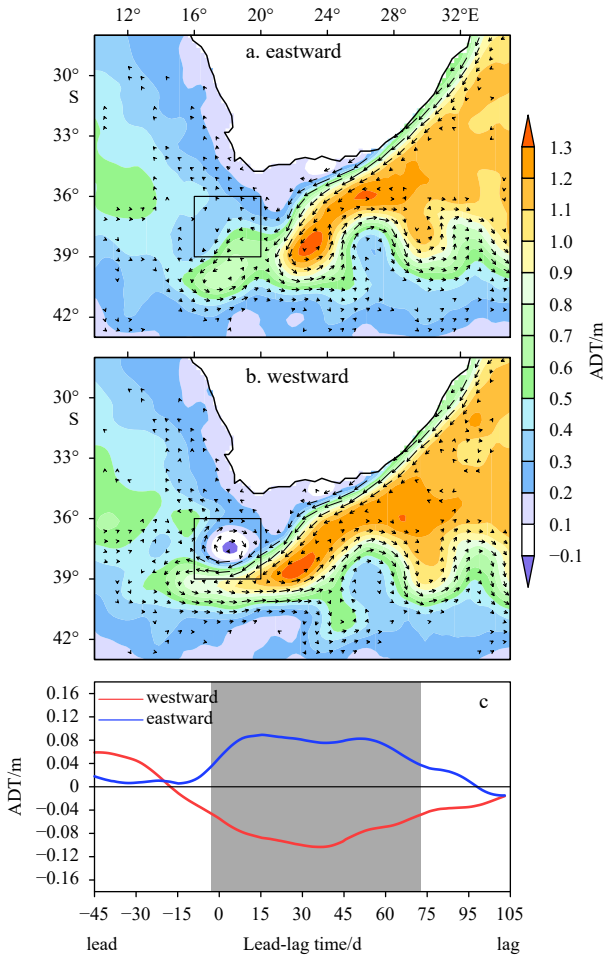

Fig. 5. Absolute dynamic topography (ADT) on the north side are associated with the retroflection position. a and b. The composites of the ADT for the 24 most eastward and the 21 most westward retroflection months. In a and b the black vectors denote the corresponding surface velocity; the black rectangular box is approximately where a cyclonic feature coincides with the westward elongation of the AC jet path in the westward composite. c. The blue curve is the 15-d running average of the spatial mean ADT within the black box in a, 45 d before the most eastward retroflection events until 105 d afterwards; the red curve is the same but referenced to the most westward retroflection events; the grey shading in c indicates the composited differences between the westward and the eastward retroflection events are significant at the 95% confidence level of *t*-test.

The approximate area for the cyclonic feature is marked by a black rectangular box (Fig. 5b), within which the spatially averaged ADT is shown from 45 d before to 105 d after the occurrence of extreme retroflection displacements (Fig. 5c). The timing of the changes of the mean ADT within the rectangular box indicates that ADT anomalies develop almost in parallel to the east-west shift of retroflection and persist over 60 d, which fully demonstrates a close connection between the westward extension of the AC and the cyclonic anomaly at the north flank of AC axis. In contrast, the eastward shift of the retroflection is roughly associated with the overall anticyclonic anomalies on the north side. This inspired us to speculate on the other factors that drive the east-west shift of retroflection position than the aforementioned AC jet strength or its stability.

We therefore examined the possible effect of the local wind

stress curl in the vicinity of retroflection area. The composite of wind stress curl anomalies for 24 extreme eastward shift retroflection months (Fig. 6a) is generally positive in the whole region. On the contrary, the composite of the wind stress curl anomalies for westward retroflection position is mostly negative (Fig. 6b), especially around the retroflection. To examine the effect of the local wind forcing where the cyclonic feature appears (black rectangular box in Fig. 5b), the 15-d running mean wind stress curl within the box is lead-lag composited for eastward retroflection events (blue line in Fig. 6c) and westward retroflection events (red line in Fig. 6c), respectively. The positive (negative) wind

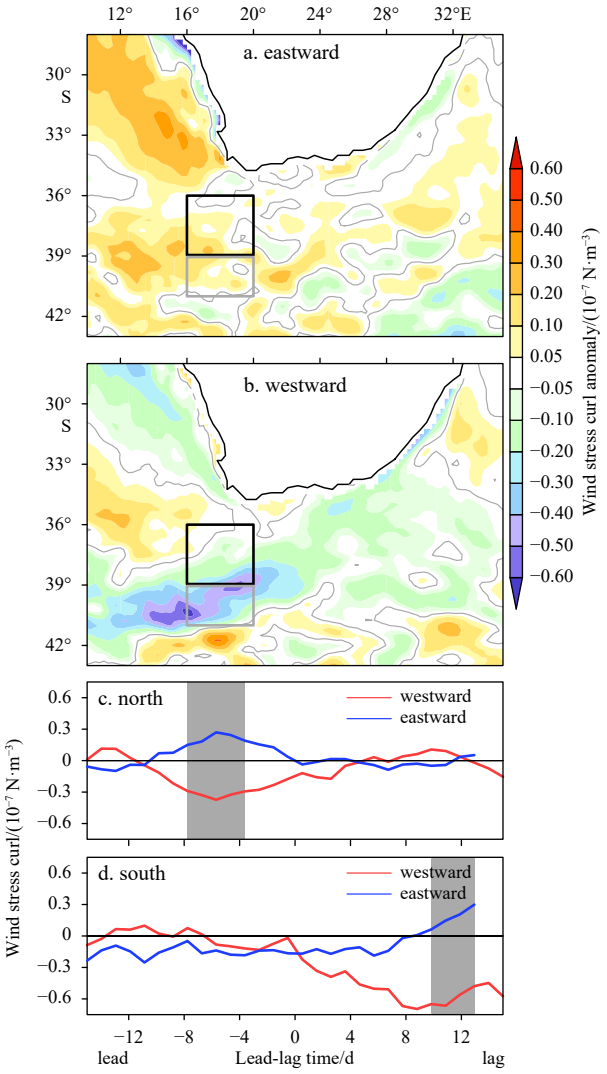

Fig. 6. Wind stress curl anomalies at the north flank lead to the retroflection position shift. a. The wind stress curl anomalies corresponding to the composite of the 24 most eastward retroflection events. b. Same as a but composite of the 21 most westward retroflection events. In a and b, the black rectangular box is approximately where a cyclonic feature coincides (same as in Fig. 5b), and the grey box is chosen to represent an area of maximal negative wind stress curl anomaly. c. 15-d moving average of the spatial mean wind stress curl in the black rectangular box to the north, from 15 d before the event till 15 d afterwards. d. Same as c but for the mean wind stress curl in the grey box to the south. The grey shading indicates the composited differences between the westward and the eastward retroflection events are significant at the 95% confidence level of *t*-test.

stress curl within the box starts developing about 10 d before the extreme eastward (westward) retroflection occurs, and its magnitude reaches a maximum about 5 d to 6 d before the extreme. The same lead-lag composite analysis is also applied to the region of retroflection (grey box in Fig. 6b), where the differences in wind stress curl composites appears the largest. In contrast, the 15-d running mean wind stress curl anomalies in this area did not exhibit any significant difference for two groups of extreme events until about 8 d after the retroflection point shift (Fig. 6d). Therefore, a wind-driven mechanism is proposed here to interpret the east-west shift of retroflection point. In response to the anomalous negative wind stress curl forcing within the black rectangular box (Fig. 6), a local cyclonic anomaly develops on the north side of the retroflection, which in turn accelerates the westward Agulhas jet stream and results in the westward shift of the retroflection. On the contrary, positive wind stress curl suppresses the anomalous cyclone, resulting in the retreat of jet stream at its southern flank and the eastward shift of retroflection.

5 Longitudinal shifts of the retroflection point induced by local wind stress

In order to verify the above inferred mechanism, a ROMS model was configured in the Agulhas system area and a set of numerical experiments were designed. The detailed choices for numerical schemes and parameters can be found in Section 2.2. Due to the pulse-like behavior of the retroflection related to ring shedding processes, timings of the retroflection positions corresponding to different local wind forcing conditions cannot be compared directly. Instead, mean retroflection longitudes on time scales longer than 1 year are compared to qualitatively verify the local wind forcing effects on the retroflection position. We firstly checked the annual mean ADT during the altimeter era (1993–2018) for the observation data. It turns out that similar patterns of cyclonic features are present in certain years, while absent in others. Here the two contrasting years of 2017 and 2002 are selected (shown in Fig. 7) because the mean retroflection longitudes in these two years are relative eastward (18.4°E) and westward (17.7°E). It is noteworthy that a cyclonic feature is present at the northern flank of the westward extension of the AC in 2002 (Fig. 7b), but not in 2017 (Fig. 7a). In association with the obvious ADT contrast, the annual mean wind stress curl anom-

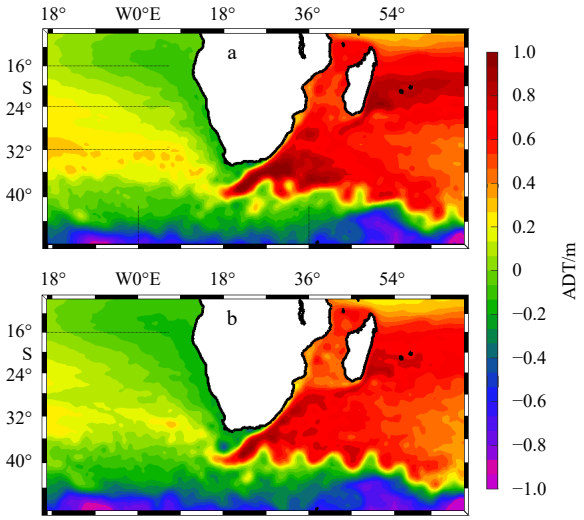

Fig. 7. The mean absolute dynamic topography (ADT) derived from altimetry data in 2017 (a) and 2002 (b). Notice the cyclone to the north of the retroflection point in 2002.

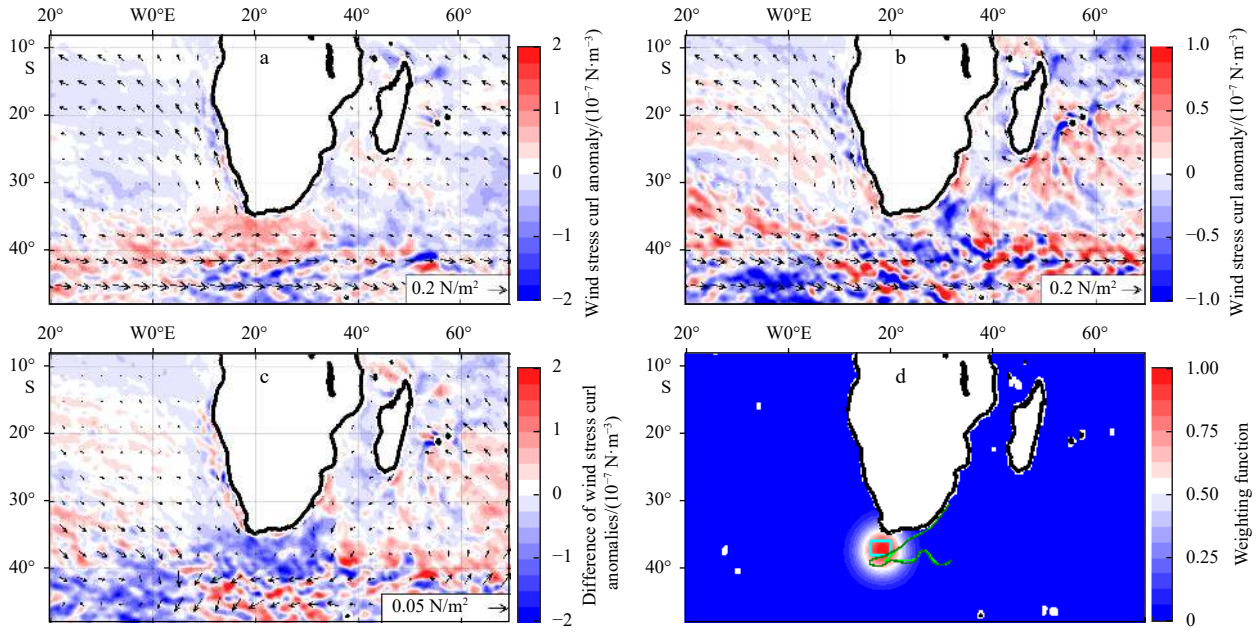

Fig. 8. Configurations of the wind forcing for numerical experiments. The anomaly of the ERA5 wind stress curl and 10 m wind stress vector in 2017 (a) and 2002 (b), referenced to the 1979 to 2019 climatology. The difference between a and b is shown in c. d. Non-dimensional weighting function, which will be multiplied to the wind stress difference (2002–2017) and then added to the Case1 forcing to produce the perturbed run (Case 2). The cyan box is approximately where a cyclonic feature coincides (same as the black rectangular box in Figs 6a and b), and the dark and light green contours represent the mean sea surface height to indicate the retroflection position for the year of 2017 and 2002, respectively.

alies in these two years also exhibit a great contrast between the positive anomalies in 2017 (Fig. 8a) and the negative anomalies in 2002 (Fig. 8b), particularly in the retroflection region. Therefore, the possible connection between negative wind stress curl anomalies, cyclonic circulation, and the westward extension of retroflection position may work even in annual mean state, i.e., 2002. And the opposite process may occur in other years such as 2017, with positive wind stress curl anomalies corresponding to the inactive cyclone and the eastward shift of retroflection.

In view of the significant differences between these two years (Figs 8a and b), the mean state, the boundary conditions, and the surface forcings in 2017 were used to spin up the model and drive the control run, whereas perturbed local wind stress is used to drive three perturbed runs. Three steps were implemented to generate the perturbe local wind stress. First, the mean wind stress forcing in 2017 was subtracted from the mean wind stress in 2002 (Fig. 8c). Second, the local wind stress anomaly was obtained, by multiplying the difference with a gaussian weighting function $W(x, y)$ varying in space as follows:

$$W(x,y) = \exp\left[-\frac{(x-x_0)^2 + (y-y_0)^2}{R^2}\right], \quad (4)$$

where the center (x_0, y_0) is at 18.5°E, 37.25°S, and R is 350 km, and its spatial distribution is shown in Fig. 8d. Third, the wind stress anomaly is added to the mean wind stress in 2017, which is used to force three perturbed runs. The parameters of the weighting function are chosen so that a strong negative wind stress curl anomaly close to that in 2002 is applied roughly within the rectangular box to the north of the retroflection (Fig. 8d), while other area of the domain is still forced by the 2017 mean wind stress.

The model was spun up by applying 2017 mean ERA5 surface wind stress, heat flux, and radiation flux for 10 years, with 2017 mean ORAs5 temperature, salinity, and velocity as boundary conditions. The end of spin-up state is used as initial condition, and the same surface forcings are applied for another 5 years as the "control" run. Then three "perturbed" runs are performed for 5 years, with the same forcing as the control run, except that the local wind stress perturbations are applied with 0, 1, and 2 months dalay after the control run. In this way, we can examine an ensemble of the longitudinal retroflection shift runs, so as to minimize the bias due to intermittent ring shedding and ensure robustness of the results.

The modeled 5-year mean SSH for the control run and the ensemble mean SSH of the three perturbed run are shown in Figs 9a and b. The modeled Agulhas Current transports are calculated by integrating the cross-ACT (Agulhas Current Time-series) instrumental array (Beal and Elipot, 2016) transports within 1 000 m depth, and the resulting AC transports are $(74.8 \pm 11.3) \times 10^6$ m^3/s for the control run, and $(74.7 \pm 11.9) \times 10^6$ m^3/s, $(75.6 \pm 12.3) \times 10^6$ m^3/s, $(75.3 \pm 12.8) \times 10^6$ m^3/s for the three perturbed runs respectively. The transports are consistent to the AC transport estimated by previous studies, e.g., 73.0×10^6 m^3/s in Beal and Bryden (1999). The AC transports are not significantly different between the control run and the perturbed runs, hence cannot be the likely cause of the retroflection shifts. The three perturbed runs are forced with a cyclonic wind stress curl anomaly in an area adjacent to the retroflection (Fig. 8d). Although the model is not able to simulate the cyclonic feature as observed (Fig. 7b), the SSH difference between perturbed runs and the control runs within the cyan box (Fig. 8d) is more than 0.1 m. The absence of the cyclonic eddy is probably because the model resolution cannot resolve the submesoscale processes (Schubert et al., 2021). Nevertheless, a notable discrepancy of retroflection positions between these two cases can be easily detected, i.e., 17.5°E for the control run, and 16.8°E, 17.1°E, and 17.2°E for the perturbed runs. A closer look at the retroflection area shows that the retroflection of the ensembled perturbed runs locate further west than the control run (Figs 9a and b).

Due to the intermittent pulsing of the retroflection associated with ring shedding, a few extreme retroflection events can render a huge shift of the mean retroflection on seasonal to interannual time scales. Therefore, instead of directly examining the retroflection time series, the probability distribution of the retroflection longitudes are compared between the control run and the perturbed runs (Figs 9c and d). The retroflection longitudes for each model run is calculated using the kinematic algorithm proposed in Section 2.3, based on 3-d average horizontal velocity. The total number of occurances of retroflection are counted in bins from 13°E to 25°E with 1° increment, and are divided by the total number of occurances in all bins from 13°E to 25°E to derive the probability distribution of the retroflection longitudes. In the first 3 model years, the most probable retroflection longitudes for the perburbed runs are further west, resulting in more westward mean retroflection longitudes in the perturbed runs than in the control run (Fig. 9c). While for the latter 2 years, the most probable retroflection longitudes for the perturbed runs are not consistently further west than the control run (Fig. 9d). The consistency of the westward retroflection shift is abscent when the local forcing is prolonged than 3 years, indicating that local cyclonic wind stress perturbation may not have a lasting effect. On the contrary, the large-scale westerly changes beyond the retroflection may cause a more sustained shift of retroflection and more profound circulation adjustment (Durgadoo et al., 2013).

Although the local wind stress anomaly in the model did not generate the strong oceanic cyclonic feature to the north of the retroflection, the ocean responses can still lead to the westward retroflection shift. This discrepancy between model and observation results may be interpreted by local negative relative vorticity anomalies to the north of the retroflection in the perturbed runs in contrast with the control run (figure not shown), which corresponds to southwestward advection and possibly leads to prolonged AC and more westward retroflection in the purburbed runs. This analysis indicates that even though the cyclonic feature does not prominently show up in numerical experiment, the local negative wind stress anomaly indeed can induce local negative vorticity anomaly and the westward retroflection shift through ocean advection. The experiment results indicate that in the real ocean, the local wind stress forcing may play an even more important role in determining the retroflection location.

6 Possible linkage of the retroflection position and Agulhas ring shedding

Strong eddy activities have been observed in close proximity to the retroflection, as a result of the retroflection shifting as well as eddy spawning (Fig. 1b). The composite ADT of the extremely westward retroflection clearly show a cyclonic circulation at the north (Fig. 5b), which may play a role in the processes of Agulhas ring shedding and Indian-to-Atlantic Ocean volume transport. To preliminarily examine the possible connection of this cyclonic feature, Agulhas ring shedding and the AL, lead-lag composite analysis of 15-d mean ADT based on the retroflection position index is done and shown in chronological order in Fig. 10 for the westward shift and Fig. 11 for the eastward shift of retroflection events.

A weak cyclonic feature can be identified 30 d before the extreme westward retroflection occurs (Fig. 10a), and it gradually strengthens as the retroflection intrudes westwards (Figs 10b, c, and d). Then the cyclonic feature can last about 60 d on average after the extreme westward retroflection occurs (Fig. 5c). After the retroflection reaches the westernmost longitude, an Agulhas ring develops and sheds as the retroflection retreats back to the Indian Ocean (Figs 10e and f). In the extreme westward retroflection cases, the presence of the long-lasting cyclonic feature as well as the more westward shedding location of the Agulhas ring may make it easier for the rings to propagate further northwestward into the Atlantic, and resulting in higher AL.

Before the occurrence of extreme eastward retroflection events, the similar weak cyclonic feature can also be clearly identified at the north flank of the retroflection region (Figs 11a and b). This cyclone, however, shifts southwestward and decays with

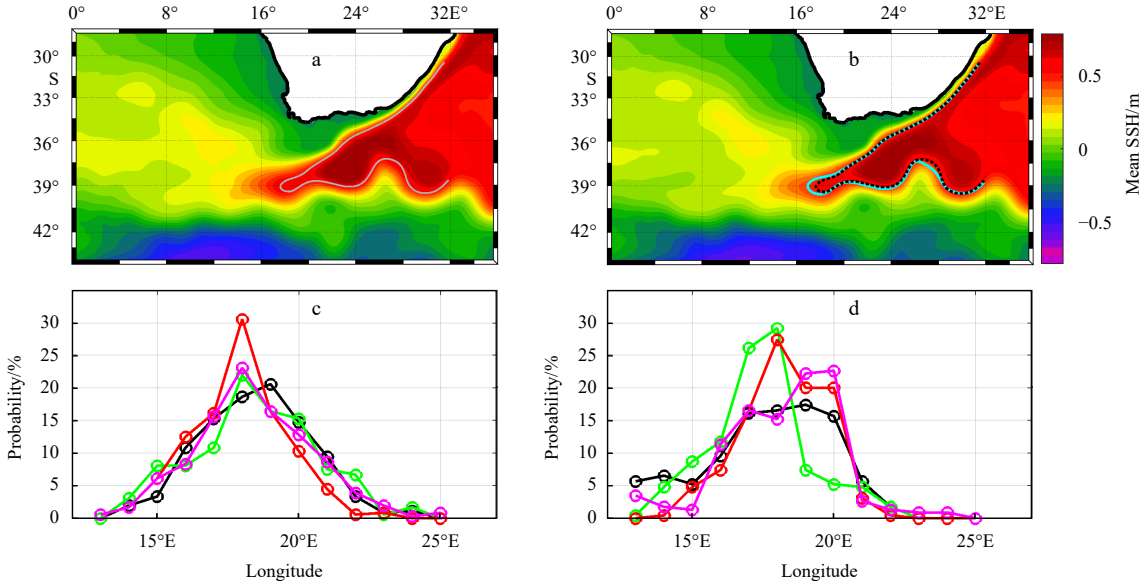

Fig. 9. Modeled longitudinal position of the retroflection. Mean sea surface height (SSH) in the retroflection area from control run forced by 2017 mean wind stress (a) and the ensemble of the three perturbed runs forced by 2017 wind stress plus a local 2002 anomaly around the retroflection area (b). The black dashed curve represents the 0.5 m SSH isoline for the control run, and the cyan curve represents the 0.5 m SSH isoline for the ensembled perturbed runs. c. The probability distribution of the retroflection longitudes for the first three model years, the black curve and circles represent the control run, while the magenta, the green, and the red represent the three perturbed runs. d. Same as c, but the result from the latter two model years.

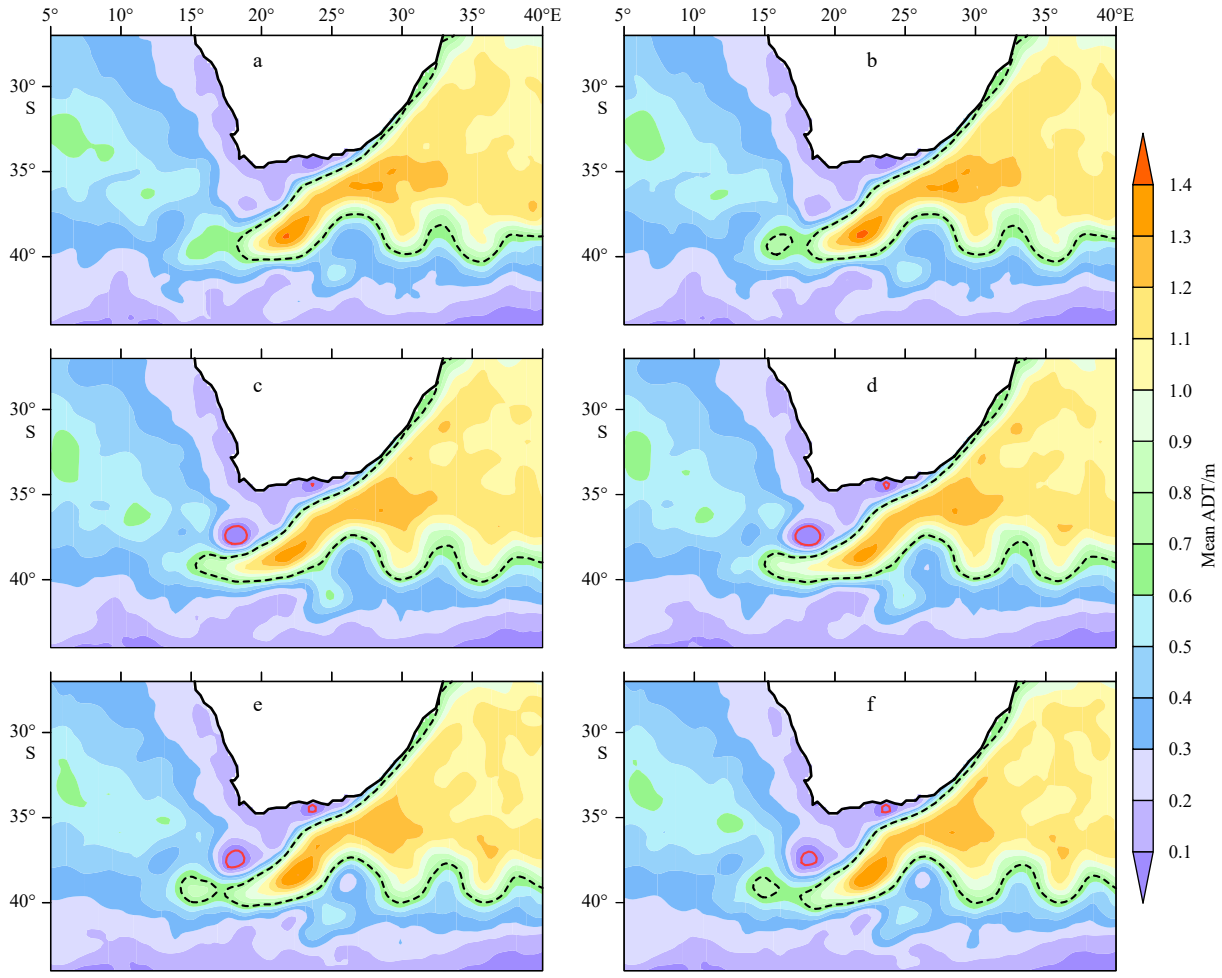

Fig. 10. Time evolution of Agulhas ring shedding process for the westward retroflection events. The composite of 15-d mean ADT leading to extreme westward retroflection events. a. Mean ADT over the period 30 d to 15 d before the extreme eastward retroflection events. b and c. Same as a, but from 22 d to 7 d, and 15 d to 0 d before the extreme westward retroflection events respectively. d. Mean ADT from 8 d before the event to 7 d after the event. e and f. Same as d, but for the mean ADT from the day of the event to 15 d afterwards and from 16 d to 23 d after the event, respectively. Red solid contours include areas of negative ADT value. Black dashed lines indicate the 0.7 m ADT value, which has been usually used to estimate the retroflection position.

time, in association to the retreat of the AC axis and ring shedding event (Figs 11c and d). It seems that the weakened cyclone, on its way southwestward, blocks the movement of the newly formed ring, resulting in the reintegration of the ring into the continuously westward advancing AC jet (Figs 11e and f). Although we cannot definitely conclude that all of rings shedding in the extreme eastward retroflection events are merged back again into the AC, these composite results at least allude less rings propagating into the Atlantic, hence weaker AL for the eastward retroflection months.

It is worth noting that the Agulhas leakage is not merely composed of Agulhas rings, but includes the mean flow, the mesoscale eddies and the filaments. Rühs et al. (2022) integrated multi-source data to examine the long-term change of the AL. They asserted that on the decadal time scale, the AL is attributed less to the Agulhas rings and the EKE, but more to the mean flow. In order to probe possible impact of the retroflection position on the Atlantic water property on monthly scale, the OISST anomaly and ERA5 SST anomaly (SSTa) are composited on the retroflection position index (Fig. 12). With the retroflection shifting westward, the remarkable warming on the South Atlantic side (solid box in Fig. 12, hereafter SA) is in sharp contrasts to the moderate cooling on the Indian Ocean side (dashed box in Fig.12, hereafter IO). The retroflection-related SST anomalies are insensitive to the dataset selection (Figs 12a and b), and can persist to the next month (Fig. 12c). This result is consistent with the study of Zhu et al. (2021), though they applied different method of retroflection identification. According to Biastoch et al. (2015) and Rühs et al. (2022), the SST difference between the SA and the IO can be viewed as a good proxy for the AL variability (hereafter AL_{SST}). Figure 13 shows the lead-lag composited differences of the AL_{SST} based on the retroflection index. It is apparent that the westward retroflection events are associated with the positive anomalous AL (red crosses) within two months, while the eastward retroflection cases are followed by the weakening AL (blue circles) in the next month (Fig. 13a). The resultant AL_{SST} differences between the westward and the eastward retroflection events are significantly beyond the standard error bars in the time lag of zero and one month (Fig. 13b). This lends the support for the monthly to seasonal correspondance of the AL variability with the retroflection position via the Agulhas ring shedding process.

To further verify the inference from the above composite analysis, we selected several extreme cases to check their ring shedding processes one by one. As shown in Fig. 14, left panels are two eastward retroflection cases and right panels are two west-

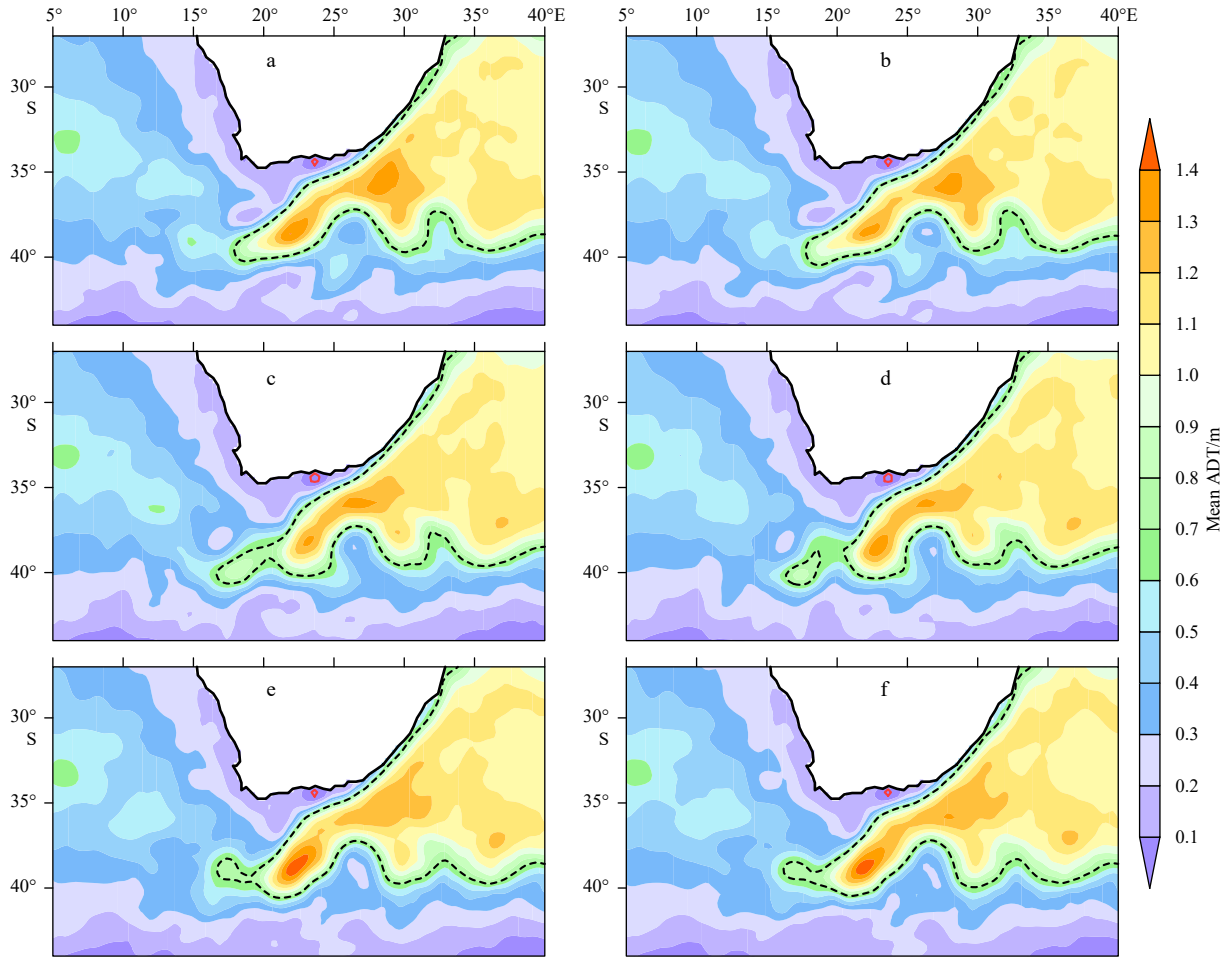

Fig. 11. Time evolution of Agulhas ring shedding process for the eastward retroflection events. The composite of 15-d mean ADT leading to extreme eastward retroflection events . a. Mean ADT over the period 30 d to 15 d before the extreme eastward retroflection events. b and c. Same as a, but from 22 d to 7 d, and 15 d to 0 d before the extreme westward retroflection events respectively. d. Mean ADT from 8 d before the event to 7 d after the event. e and f. Same as d, but for the mean ADT from the day of the event to 15 d afterwards and from 16 d to 23 d after the event, respectively. Red solid contours include areas of negative ADT value. Black dashed lines indicate the 0.7 m ADT value, which has been usually used to estimate the retroflection position.

ward retroflection cases according to our criteria. Their corresponding AC jet paths are plotted as red thick lines. In consistent with the previous studies (Zhu et al., 2021), the 0.7 m ADT isolines (colored contours) are chose to ascertain the time evolution of retroflection. For the eastward retroflection cases, the disruption of isolines occurs at about 19°E for Case 1 (Fig. 14a) and about 21°E for Case 2 (Fig. 14c). The resultant rings, however, keep relatively still and stable for weeks, until they are absorbed into the main flow. This may lead to the abrupt westward jump of retroflection position within the framework of ADT/SSH contour criteria. For the westward retroflection cases, the rings fall off the main flow west of 18°E (Figs 14b and d), and they continuously move westward into the Cape Basin in 30 d. The strong contrast of ring activity between the eastward and the westward cases lend support to the composite results, alluding to the connection of retroflection position and the AL on monthly timescale.

7 Summary and discussions

In this study, a kinematic criterion based on the spatial distribution of MKE and EKE is proposed to ascertain the AC strength, its stability as well as the retroflection position within an unified framework. Their linear correlations are examined and the result suggests decoupling of the retroflection position and the AC. Further composite analyses reveal that a cyclonic feature north of the retroflection, possibly induced by the local wind stress curl, is closely associated with the extreme westward retroflection events. Numerical experiments are then designed to test whether and how much local wind stress anomaly can affect the AR displacements. The simulated mean retroflection longitudes, forced by local negative wind stress anomaly, have shifted westward significantly. Furthermore, our results suggest the different fates of detached rings corresponding to the shift of retroflection, i.e., reabsorbed into the mean flow for the easternmost retroflection or migrating persistently towards the Atlantic Ocean for the westernmost retroflection. This also indicates the relevance of AR position to the AL because the passage of Agulhas rings can result in pronounced AL events (Cheng et al., 2016).

Due to the turbulent activities in the retroflection area, especially in the processes of ring generation, migration and dissipation, ambiguity is inevitable for the retroflection identification. Most of previous studies have simply chosen a fixed SSH as a critical value and took the westernmost grid point on the corresponding isoline as the retroflection. The retroflection longitude obtained this way is thus very sensitive to the chosen critical value. For instance, the difference between retroflection locations obtained using 1.7 m and 1.9 m as critical SSH is in the

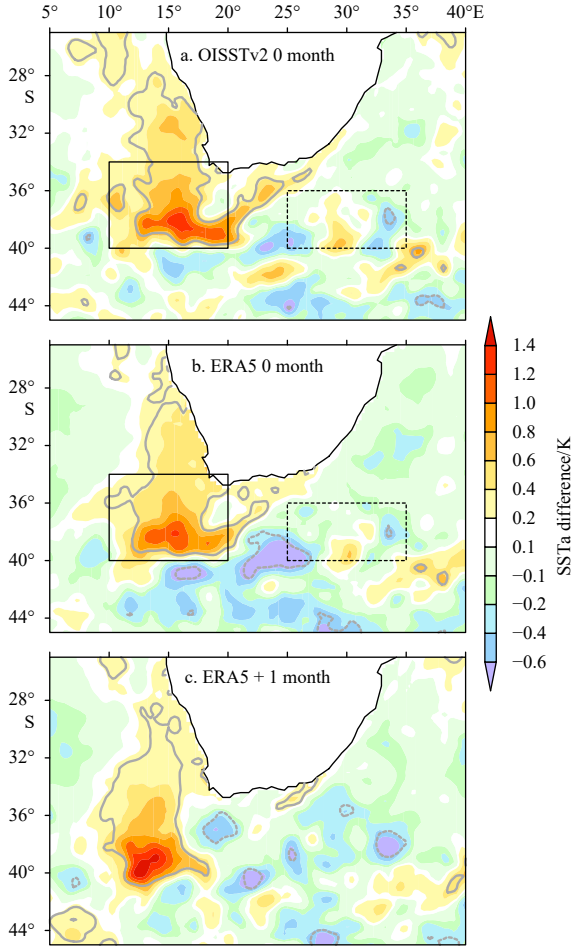

Fig. 12. Westward retroflection leads to warming in the South Atlantic (SA) and cooling in the Indian Ocean (IO), corresponding to the enhanced Agulhas leakage. Composited monthly SSTa differences between the westward and the eastward retroflection events from OISST dataset (a) and EAR5 dataset (b). c. Same as b, but with SSTa lag retroflection events for one month. The grey contours include the areas where the differences are significant at 95% confidence level of *t*-test. The black solid and dashed rectangular boxes denote the SA region and the IO region, respectively.

range of 30 km to 150 km most of the time, but can be as large as 600 km (Dencausse et al., 2010a). More importantly, the unstable state of AC jet path downstream makes it difficult to distinguish exact retroflection position from temporary isoline disruptions in a morphological perspective. For example, an extreme eastward retroflection event of 2000/2001 has been noted in previous studies (de Ruijter et al., 2004; Dencausse et al., 2010a). The event lasts nearly half a year, resulting in zero ring shedding and greatly reduced AL. However, none of these months stands out in this study as the easternmost retroflection cases. A detailed probe in-

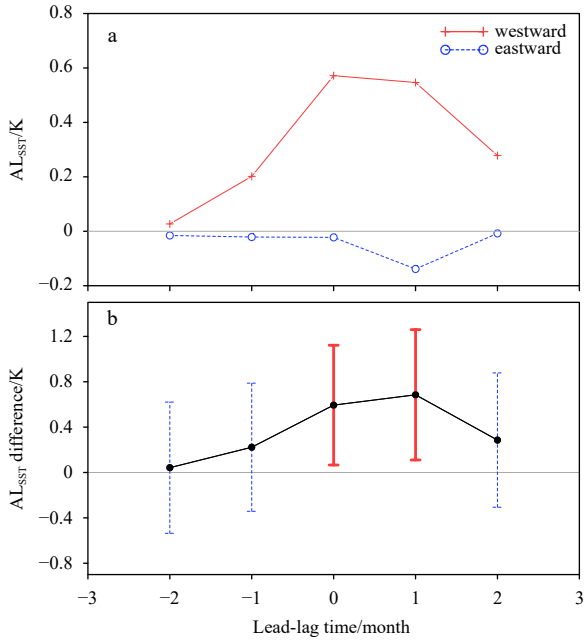

Fig. 13. Significant differences between the westward and eastward retroflection events in AL_{SST}. a. Lead-lag compositions of ERA5 AL_{SST} for the westward retroflection events (red crosses) and for the eastward retroflection events (blue circles). The AL_{SST} is computed from the difference between the SA (solid box in Fig. 12) mean SST anomalies and the IO (dashed box in Fig. 12) mean SST anomalies. b. The AL_{SST} differences between the westward and the eastward retroflection differences are statistically significant at 95% confidence level of *t*-test, whereas the values overlapped by the blue dashed bars are insignificant.

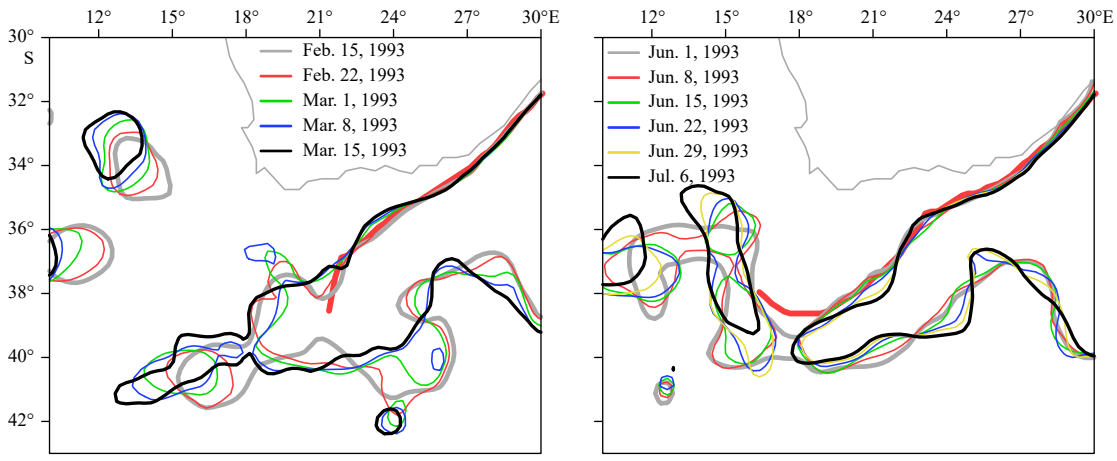

a. east Case 1 (Feb. 1993)　　b. west Case 1 (Jun. 1993)

Fig. 14

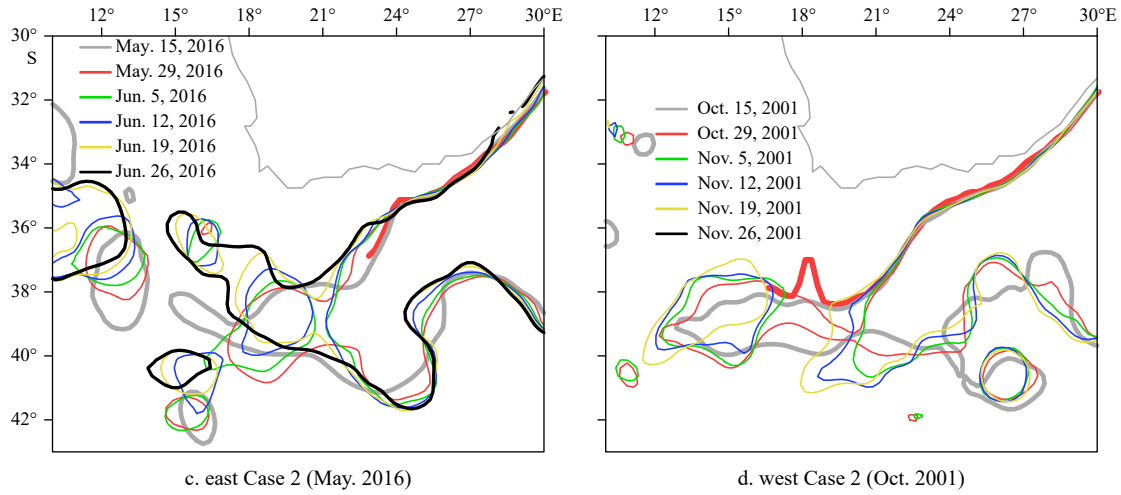

c. east Case 2 (May. 2016) d. west Case 2 (Oct. 2001)

Fig. 14. Time evolution of Agulhas ring shedding processes for four extreme retroflection cases. The 15-d mean 0.7 m ADT contours are plotted every 7 d or 14 d in different colors. The thick red lines denote the positions of AC axis. For two extreme eastward retroflection cases, the ring shedding processes occur at 19°E (a) and 21°E (c) and the rings are both re-merged into the main flow in about 30–40 d. For two extreme westward retroflection cases (b and d), the ring shedding processes occur at 15°–18°E and the rings both move westward.

to the event reveals that the ADT isoline indeed breaks up at about 28°E at the end of November (Fig. 15a). The water body falling off the main flow remains essentially stable for over three months (Figs 15b, c and d), neither westward drifting nor re-mer-

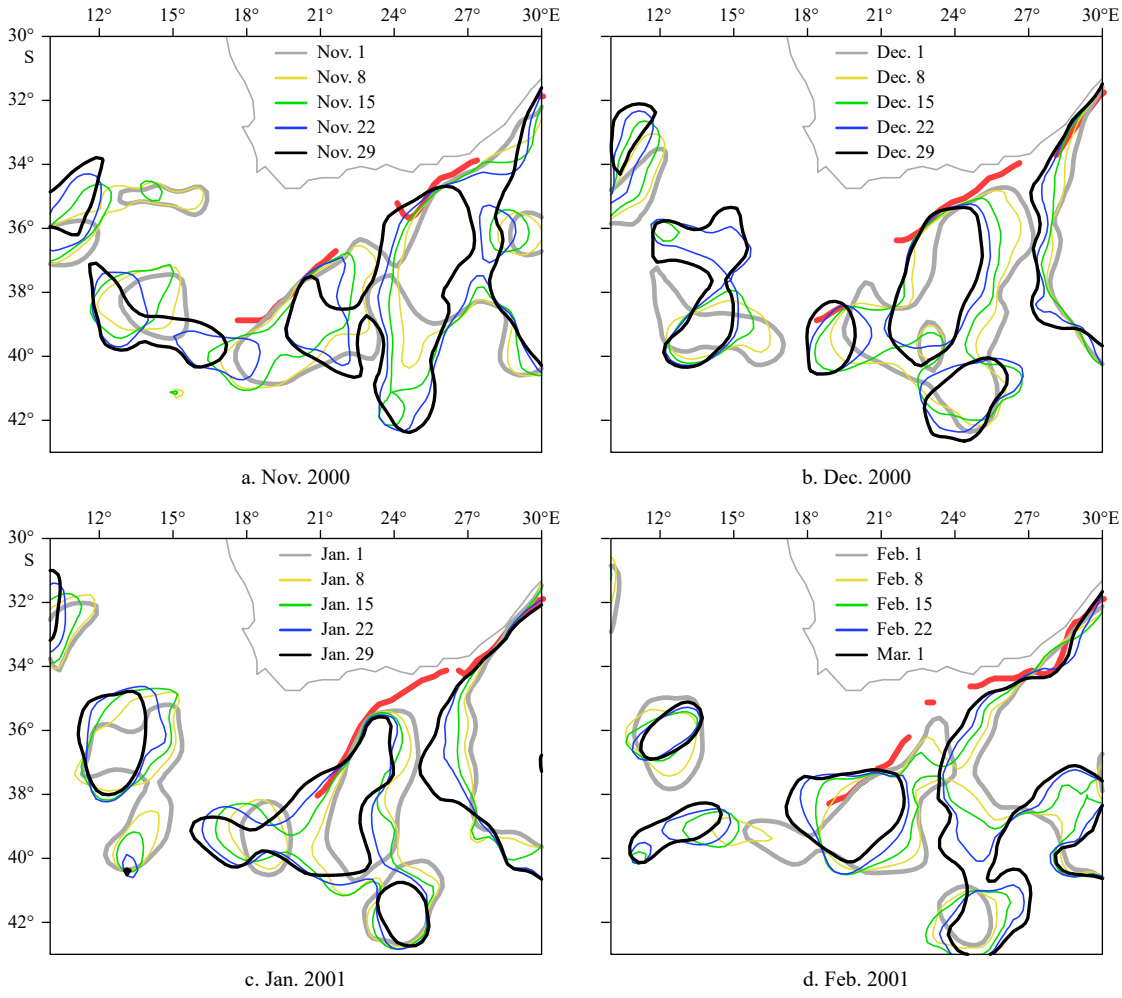

a. Nov. 2000 b. Dec. 2000

c. Jan. 2001 d. Feb. 2001

Fig. 15. Time evolution of Agulhas ring shedding processes for the extreme early (eastward) retroflection during November 2000 to February 2001 recorded by Dencausse et al. (2010a). a. November 2000; b. December 2000; c. January 2001; d. February 2001.

ging into the mainstream. Therefore, the controversy about the retroflection point lies in whether this water body belongs to or is independent from the AC mainstream. In consideration of the strong stability and large size of the fractured body, it is rational to regard the body as a part of AC, thus the retroflection point could be set at the west end of fractured body (about 18°–21°E) rather than at its east end (about 27°–28°E). This inference can be further evidenced by a fragmented but extended AC path far beyond 27°E according to our kinematic standard (red thick lines in Fig. 15). In this sense, the 2000/2001 event should not be grouped into the easternmost retroflection events from a dynamical perspective, though in morphology it appears an early retroflection.

The pulsation of the retroflection has been noted previously (Lutjeharms and van Ballegooyen, 1988), and is mostly characterized by a westward progression lasting 25.7 d on average followed by abrupt eastward shift (Dencausse et al., 2010a). In this study, the westernmost retroflection is unstable to form rings, and the subsequent eastward retreat of the retroflection makes it hard to reabsorb the ring but to let it shed. The easternmost retroflection may also form rings as it grows unstable, but it tends to reabsorb the ring during its subsequent westward protrusion. Our study is roughly consistent with findings by Dencausse et al. (2010a) that most complete separations of ring from the AR coincides with the westward extremes in spite of the discrepancy in the AR position estimation. Since AL occurs mostly in the form of Agulhas rings, it can be inferred that the leakage is much larger during the westward retroflection than the eastward cases in monthly and annual timescale, which is partly supported by our numerical experiments. This may set a new theoretical base to investigate the AL variation on multiple time scales. Nonetheless, further statistical and modelling studies are necessary to establish a robust physical connection and quantitative relation between the AR and the AL, which can greatly improve our understanding of inter-basin exchange in the Southern Ocean as well as its role in the AMOC variability and in the global climate change.

References

Backeberg B C, Penven P, Rouault M. 2012. Impact of intensified Indian Ocean winds on mesoscale variability in the Agulhas system. Nature Climate Change, 2(8): 608–612, doi: 10.1038/nclimate1587

Beal L M, Bryden H L. 1999. The velocity and vorticity structure of the Agulhas Current at 32°S. Journal of Geophysical Research: Oceans, 104(C3): 5151–5176, doi: 10.1029/1998JC900056

Beal L M, Elipot S. 2016. Broadening not strengthening of the Agulhas Current since the early 1990s. Nature, 540(7634): 570–573, doi: 10.1038/nature19853

Biastoch A, Böning C W, Lutjeharms J R E. 2008. Agulhas leakage dynamics affects decadal variability in Atlantic overturning circulation. Nature, 456(7221): 489–492, doi: 10.1038/nature07426

Biastoch A, Böning C W, Schwarzkopf F U, et al. 2009. Increase in Agulhas leakage due to poleward shift of Southern Hemisphere westerlies. Nature, 462(7272): 495–498, doi: 10.1038/nature08519

Biastoch A, Durgadoo J V, Morrison A K, et al. 2015. Atlantic multidecadal oscillation covaries with Agulhas leakage. Nature Communications, 6(1): 10082, doi: 10.1038/ncomms10082

Bryden H L, Beal L M, Duncan L M. 2005. Structure and transport of the Agulhas Current and its temporal variability. Journal of Oceanography, 61(3): 479–492, doi: 10.1007/s10872-005-0057-8

Byrne D A, Gordon A L, Haxby W F. 1995. Agulhas eddies: a synoptic view using Geosat ERM data. Journal of Physical Oceanography, 25(5): 902–917, doi: 10.1175/1520-0485(1995)025<0902:AEASVU>2.0.CO;2

Cheng Yu, Putrasahan D, Beal L, et al. 2016. Quantifying Agulhas leakage in a high-resolution climate model. Journal of Climate, 29(19): 6881–6892, doi: 10.1175/JCLI-D-15-0568.1

Daher H, Beal L M, Schwarzkopf F U. 2020. A new improved estimation of Agulhas leakage using observations and simulations of lagrangian floats and drifters. Journal of Geophysical Research: Oceans, 125(4): e2019JC015753, doi: 10.1029/2019JC015753

de Ruijter W P M, Biastoch A, Drijfhout S S, et al. 1999. Indian-Atlantic interocean exchange: dynamics, estimation and impact. Journal of Geophysical Research: Oceans, 104(C9): 20885–20910, doi: 10.1029/1998JC900099

de Ruijter W P M, van Aken H M, Beier E J, et al. 2004. Eddies and dipoles around South Madagascar: formation, pathways and large-scale impact. Deep Sea Research Part I: Oceanographic Research Papers, 51(3): 383–400, doi: 10.1016/j.dsr.2003.10.011

Dencausse G, Arhan M, Speich S. 2010a. Spatio-temporal characteristics of the Agulhas Current retroflection. Deep Sea Research Part I: Oceanographic Research Papers, 57(11): 1392–1405., doi: 10.1016/j.dsr.2010.07.004

Dencausse G, Arhan M, Speich S. 2010b. Routes of Agulhas rings in the southeastern Cape Basin. Deep Sea Research Part I: Oceanographic Research Papers, 57(11): 1406–1421, doi: 10.1016/j.dsr.2010.07.008

Dijkstra H A, de Ruijter W P M. 2001. On the physics of the Agulhas Current: steady retroflection regimes. Journal of Physical Oceanography, 31(10): 2971–2985, doi: 10.1175/1520-0485(2001)031<2971:OTPOTA>2.0.CO;2

Durgadoo J V, Loveday B R, Reason C J C, et al. 2013. Agulhas leakage predominantly responds to the Southern Hemisphere westerlies. Journal of Physical Oceanography, 43(10): 2113–2131, doi: 10.1175/JPO-D-13-047.1

Feron R C V, de Ruijter W P M, Oskam D. 1992. Ring shedding in the Agulhas Current system. Journal of Geophysical Research: Oceans, 97(C6): 9467–9477, doi: 10.1029/92JC00736

Gunn K L, Beal L M, Elipot S, et al. 2020. Mixing of subtropical, central, and intermediate waters driven by shifting and pulsing of the Agulhas Current. Journal of Physical Oceanography, 50(12): 3545–3560, doi: 10.1175/JPO-D-20-0093.1

Haidvogel D B, Arango H G, Hedstrom K, et al. 2000. Model evaluation experiments in the North Atlantic Basin: simulations in nonlinear terrain-following coordinates. Dynamics of Atmospheres and Oceans, 32(3/4): 239–281, doi: 10.1016/S0377-0265(00)00049-X

Hersbach H, Bell B, Berrisford P, et al. 2020. The ERA5 global reanalysis. Quarterly Journal of the Royal Meteorological Society, 146(730): 1999–2049, doi: 10.1002/qj.3803

Le Bars D, de Ruijter W P M, Dijkstra H A. 2012. A new regime of the Agulhas Current retroflection: turbulent choking of Indian-Atlantic leakage. Journal of Physical Oceanography, 42(7): 1158–1172, doi: 10.1175/JPO-D-11-0119.1

Loveday B R, Durgadoo J V, Reason C J C, et al. 2014. Decoupling of the Agulhas leakage from the Agulhas Current. Journal of Physical Oceanography, 44(7): 1776–1797, doi: 10.1175/JPO-D-13-093.1

Loveday B R, Penven P, Reason C J C. 2015. Southern annular mode and westerly-wind-driven changes in Indian-Atlantic exchange mechanisms. Geophysical Research Letters, 42(12): 4912–4921, doi: 10.1002/2015GL064256

Lutjeharms J R E, Boebel O, Rossby H T. 2003. Agulhas cyclones. Deep Sea Research Part II: Topical Studies in Oceanography, 50(1): 13–34, doi: 10.1016/S0967-0645(02)00378-8

Lutjeharms J R E, van Ballegooyen R C. 1988. The retroflection of the Agulhas Current. Journal of Physical Oceanography, 18(11): 1570–1583, doi: 10.1175/1520-0485(1988)018<1570:TROTAC>2.0.CO;2

Marchesiello P, McWilliams J C, Shchepetkin A. 2003. Equilibrium structure and dynamics of the California Current System. Journal of Physical Oceanography, 33(4): 753–783, doi: 10.1175/1520-0485(2003)33<753:ESADOT>2.0.CO;2

McMonigal K, Beal L M, Elipot S, et al. 2020. The impact of meanders, deepening and broadening, and seasonality on Agulhas Current temperature variability. Journal of Physical Ocean-

ography, 50(12): 3529–3544, doi: 10.1175/JPO-D-20-0018.1
Mulet S, Rio M H, Etienne H, et al. 2021. The new CNES-CLS18 global mean dynamic topography. Ocean Science, 17(3): 789–808, doi: 10.5194/os-17-789-2021
Ou H W, de Ruijter W P M. 1986. Separation of an inertial boundary current from a curved coastline. Journal of Physical Oceanography, 16(2): 280–289, doi: 10.1175/1520-0485(1986)016<0280:SOAIBC>2.0.CO;2
Reynolds R W, Smith T M, Liu C Y, et al. 2007. Daily high-resolution-blended analyses for sea surface temperature. Journal of Climate, 20(22): 5473–5496, doi: 10.1175/2007JCLI1824.1
Rio M H, Santoleri R. 2018. Improved global surface currents from the merging of altimetry and sea surface temperature data. Remote Sensing of Environment, 216: 770–785, doi: 10.1016/j.rse.2018.06.003
Rouault M, Penven P, Pohl B. 2009. Warming in the Agulhas Current system since the 1980's. Geophysical Research Letters, 36(12): L12602
Russo C S, Lamont T, Krug M. 2021. Spatial and temporal variability of the Agulhas retroflection: Observations from a new objective detection method. Remote Sensing of Environment, 253: 112239, doi: 10.1016/j.rse.2020.112239
Rühs S, Schmidt C, Schubert R, et al. 2022. Robust estimates for the decadal evolution of Agulhas leakage from the 1960s to the 2010s. Communications Earth & Environment, 3: 318
Schouten M W, de Ruijter W P M, van Leeuwen P J, et al. 2000. Translation, decay and splitting of Agulhas rings in the southeastern Atlantic Ocean. Journal of Geophysical Research: Oceans, 105(C9): 21913–21925, doi: 10.1029/1999JC000046
Schubert R, Gula J, Biastoch A. 2021. Submesoscale flows impact Agulhas leakage in ocean simulations. Communications Earth & Environment, 2(1): 197
Shchepetkin A F, McWilliams J C. 2005. The regional oceanic modeling system (ROMS): a split-explicit, free-surface, topography-following-coordinate oceanic model. Ocean Modelling, 9(4): 347–404, doi: 10.1016/j.ocemod.2004.08.002
Taburet G, Sanchez-Roman A, Ballarotta M, et al. 2019. DUACS DT2018: 25 years of reprocessed sea level altimetry products. Ocean Science, 15(5): 1207–1224, doi: 10.5194/os-15-1207-2019
van Aken H M, van Veldhoven A K, Veth C, et al. 2003. Observations of a young Agulhas ring, Astrid, during MARE in March 2000. Deep Sea Research Part II: Topical Studies in Oceanography, 50(1): 167–195, doi: 10.1016/S0967-0645(02)00383-1
van Sebille E, Barron C N, Biastoch A, et al. 2009a. Relating Agulhas leakage to the Agulhas Current retroflection location. Ocean Science, 5(4): 511–521, doi: 10.5194/os-5-511-2009
van Sebille E, Biastoch A, van Leeuwen P J, et al. 2009b. A weaker Agulhas Current leads to more Agulhas leakage. Geophysical Research Letters, 36(3): L03601
Warner J C, Sherwood C R, Arango H G, et al. 2005. Performance of four turbulence closure models implemented using a generic length scale method. Ocean Modelling, 8(1/2): 81–113, doi: 10.1016/j.ocemod.2003.12.003
Wei Lansu, Wang Chunzai. 2023. Characteristics of ocean mesoscale eddies in the Agulhas and Tasman Leakage regions from two eddy datasets. Deep Sea Research Part II: Topical Studies in Oceanography, 208: 105264, doi: 10.1016/j.dsr2.2023.105264
Zhu Yanan, Li Yuanlong, Zhang Zhengguang, et al. 2021. The observed Agulhas retroflection behaviors during 1993–2018. Journal of Geophysical Research: Oceans, 126(12): e2021JC017995, doi: 10.1029/2021JC017995